Energy & Environmental Science

ROYAL SOCIETY OF CHEMISTRY

PAPER



Cite this: *Energy Environ. Sci.*, 2020, **13**, 1730

# Highly durable photoelectrochemical $H_2O_2$ production *via* dual photoanode and cathode processes under solar simulating and external bias-free conditions†

Tae Hwa Jeon,[a] Hyejin Kim,[a] Hyoung-il Kim *[bc] and Wonyong Choi *[ad]

This study demonstrated efficient solar-to-$H_2O_2$ conversion through a photoelectrochemical (PEC) cell that maximizes the utilization of solar energy by having double side generation of $H_2O_2$ on both the photoanode and cathode. This work was accomplished by preparing (i) efficient $BiVO_4$ (BVO) photoanodes modified with various metal dopants (Mo, W, or Cr), (ii) surface-treatment with phosphate on the as-synthesized photoanodes, and (iii) single-walled carbon nanotube (CNT) electrodes with anchored anthraquinone (AQ-CNT), a reversible $H_2O_2$-evolving catalyst that has been widely used in the $H_2O_2$ production industry. The introduction of Mo into BVO and surface phosphate treatment on BVO (P-Mo-BVO) enhanced the faradaic efficiency (FE) of $H_2O_2$ production from water oxidation and slowed the $H_2O_2$ decomposition kinetics with achieving highly durable PEC reactions over 100 h (90% photocurrent remained), while bare Mo-BVO experienced the rapid decline of the photocurrent during irradiation with the dissolution of $BiVO_4$. The utilization of AQ on the cathode made the $H_2O_2$ production by oxygen reduction highly selective and suppressed competing $H_2$ production completely. Consequently, the optimized configuration of a BVO photoanode modified with Mo (10 atom%) and phosphate and an AQ-CNT cathode enabled $H_2O_2$ production on both electrodes, yielding $H_2O_2$ production with FE values of 40–50% and ~100%, respectively, across a broad range of potentials (0.75 to 2 $V_{RHE}$) and a net $H_2O_2$ production rate of 0.66 μmol $min^{-1}$ $cm^{-2}$ at 1.0 $V_{RHE}$. This dual electrode system also successfully demonstrated $H_2O_2$ production under an external bias-free condition with a net $H_2O_2$ production rate of 0.16 μmol $min^{-1}$ $cm^{-2}$ and FE value of ~43% and ~100% for photoanodic and cathodic production, respectively. To the best of our knowledge, this is the most durable PEC system for $H_2O_2$ production obtained using a $BiVO_4$-based photoanode that enabled the simultaneous photoanodic and cathodic production of $H_2O_2$.

Received 22nd May 2019,
Accepted 14th January 2020

DOI: 10.1039/c9ee03154e

rsc.li/ees

## Broader context

Hydrogen peroxide ($H_2O_2$), a carbon-free energy carrier and an environment-friendly oxidant, has been widely applied in chemical and environmental processes. While the current industrial production process of $H_2O_2$ requires $H_2$ gas, toxic organic solvents, and high energy inputs, $H_2O_2$ production by a photoelectrochemical (PEC) method that uses sunlight, water and molecular oxygen only is a green and sustainable alternative to the conventional production method. Herein we develop an efficient PEC-based $H_2O_2$ production system that utilizes the photocurrent more efficiently by having the single charge pass in the PEC cell carry out double generation of $H_2O_2$ on both the photoanode and cathode. The proposed system consists of a modified $BiVO_4$ photoanode and an anthraquinone (AQ)-modified carbon cathode. Molybdenum doping and phosphate treatment of $BiVO_4$ facilitate the selective oxidation of $H_2O$ to $H_2O_2$ and improve its durability dramatically over 100 h with preventing the dissolution of $BiVO_4$. On the other hand, AQ anchored on the carbon cathode catalyzes selective 2-electron reduction of $O_2$ to $H_2O_2$ but suppresses the competing reaction of $H_2$ production. The proposed PEC cell that generates $H_2O_2$ on both the photoanode and cathode with the maximum current utilization efficiency should be employed for further development of efficient solar PEC-based $H_2O_2$ production systems.

[a] *Division of Environmental Science and Engineering, Pohang University of Science and Technology (POSTECH), Pohang 37673, Korea. E-mail: wchoi@postech.edu*
[b] *Department of Civil and Environmental Engineering, Yonsei University, Seoul 03722, Korea. E-mail: hi.kim@yonsei.ac.kr*
[c] *Future City Open Innovation Center, Pohang University of Science and Technology (POSTECH), Pohang 37673, Korea*
[d] *Institute for Convergence Research and Education in Advanced Technology, Yonsei University, Seoul 03722, Korea*
† Electronic supplementary information (ESI) available. See DOI: 10.1039/c9ee03154e

## Introduction

Hydrogen peroxide ($H_2O_2$) is a highly useful chemical oxidant and reagent that has been widely employed in many chemical, environmental, and energy applications.[1–3] As environmentally friendly and benign production of $H_2O_2$ is needed in industry, the development of a green synthesis method is essential. In this regard, $H_2O_2$ production *via* photocatalytic (PC) or electrochemical (EC) processes is an attractive and promising method.[4–7] The oxygen reduction reaction (ORR) is a fundamental reaction in electrochemical and photochemical energy conversion processes. $H_2O_2$ can be produced through the ORR (*i.e.*, $O_2/H_2O_2$, $E^\circ$ = 0.68 V) by a two-electron transfer pathway.[8] Of various methods, the EC system has received much attention as an effective technique that allows on-site production of $H_2O_2$ *via* the direct conversion of $O_2$ and water.[9,10] Another method that has been proposed is the photoelectrochemical (PEC) production of $H_2O_2$ through dioxygen reduction or water oxidation (*i.e.*, $H_2O_2/H_2O$, $E^\circ$ = 1.76 V).[11–17] Although PEC systems have been extensively investigated for water splitting for $H_2$ and $O_2$ production,[18–23] their applications in $H_2O_2$ production are few. Bismuth vanadium oxide ($BiVO_4$) is considered one of the most promising semiconductor materials for photoanodes owing to the suitable thermodynamic driving force for the two-electron oxidation of water to $H_2O_2$.[24,25] In addition, the bicarbonate ion ($HCO_3^-$) is essentially needed in the direct production of $H_2O_2$ from water oxidation, since the bicarbonate ion acts as a hole mediator for selective hole transfer.[12]

The anthraquinone (AQ) process is a popular process for the industrial production of $H_2O_2$.[26,27] A typical AQ process for $H_2O_2$ production follows several steps:[26] an anthraquinone (typically 2-ethylanthraquinone) is catalytically hydrogenated with catalysts (mostly palladium), forming anthrahydroquinone (AHQ), and the solution containing AHQ is separated from the catalyst. AHQ reacts with molecular oxygen from injected air and returns to its original form (AQ), simultaneously producing $H_2O_2$. The AQ process is widely used in the industry at present because it allows the achievement of high production yields of $H_2O_2$. However, it has some drawbacks including the requirement of several steps, the need for $H_2$, a noble metal catalyst, and organic solvent, and the extraction of the produced $H_2O_2$ from the catalyst solution.[28,29] A possible strategy for addressing the drawbacks of the conventional AQ process is to combine it with electrochemical ORR processes. The EC production of $H_2O_2$ is driven by the cathodic reduction of $O_2$, so the efficiency is totally dependent on the performance of the catalysts. Therefore, significant efforts have been made to discover new electrocatalysts with high selectivity and efficiency.[9,30] However, it is a major challenge to develop new catalysts that meet the requirements of cost effectiveness, high selectivity, and low onset potential at the same time. Most catalysts employed in EC systems to achieve high performance are noble metal-based catalysts; non-precious metals and metal-free catalysts still suffer from high onset potential, low activity, and low selectivity.[31,32] As an alternative to developing new catalysts, a well-known AQ process can be driven in an electrochemical system by adopting an AQ-modified electrode as a cathode.[33–35] The AQ cathode can first be electrochemically reduced into AHQ form, and then AHQ will revert to the AQ form by reacting with dioxygen in the solution, generating $H_2O_2$ at the same time.[35] This electrochemical reaction can persist without a separate regeneration step for the AQ–AHQ cycle, which is well suited for its practical applications. The AQ cathode might be employed in a PEC system that should produce $H_2O_2$ selectively.

In this work, we aim to develop a highly durable and selective PEC system that utilizes the solar photons more efficiently for the production of $H_2O_2$. By developing a Mo-modified and surface phosphate-treated $BiVO_4$ photoanode and an AQ-modified carbon cathode, both holes and electrons can be simultaneously used for $H_2O_2$ production by oxidizing $H_2O$ and reducing $O_2$, respectively, with maintaining the PEC activity over 100 h (90% photocurrent remained). Although dual electrode processes for PEC $H_2O_2$ production have been previously reported,[14,15] the previous systems lacked practicality because a chemical bias between the anode and cathode compartments (even under the electrical bias-free condition) and ice cold temperature in the electrolyte were required to achieve high efficiency for $H_2O_2$ production by preventing decomposition of $H_2O_2$ and the photoanode was not stable enough for prolonged irradiation. By developing a newly modified photoanode and cathode, not only the efficiency and selectivity of PEC $H_2O_2$ production but also the durability could be significantly enhanced to make the PEC method more practical and realistic for applications. This dual PEC system is proposed as an efficient solar process (by utilizing both holes and electrons) for the sustainable production of $H_2O_2$ for prolonged irradiation ($>$100 h).

## Experimental

### Synthesis of the metal modified-$BiVO_4$ photoanode and AQ-modified carbon cathode

All reagents and chemicals were purchased from Sigma-Aldrich (of analytical grade) and used without further purification unless otherwise stated. The $BiVO_4$ photoanodes (denoted as BVO) were synthesized *via* a metal–organic decomposition (MOD) method.[36,37] In this study, typically, 0.1 M $Bi(NO_3)_3{\cdot}5H_2O$ (98%) and 0.1 M $VO(acac)_2$ (98%) were fully dissolved in acetylacetone (2,4-pentanedione, $>$99%) under stirring in the dark over 24 h. The BVO precursor solution was dropped (35 μL $cm^{-2}$) on a fluorine-doped tin oxide (F-$SnO_2$: FTO, 10 mm × 30 mm, Pilkington Co., Ltd) substrate, which was spin coated at 3000 rpm for 30 s and then annealed at 500 °C for 10 min. This spin coating–annealing cycle was repeated until the desired thickness was obtained (typically 10 cycles; ∼130 nm). The annealing was performed for 2 h in the final cycle. For the metal-modified BVO samples, $MoO_2(acac)_2$ (bis(acetylacetonato)dioxomolybdenum(VI), ≥100%), $Na_2WO_4{\cdot}2H_2O$ (sodium tungstate dihydrate, 99%), or $Na_2Cr_2O_7{\cdot}4H_2O$ (sodium dichromate tetrahydrate, 99%) was added as a metal source in the BVO precursor solution with a 1 : 1 stoichiometric ratio of Bi : (V + metal). Surface treatment with

phosphate on the photoanode was done by a simple drop-casting and annealing process. A solution containing 0.01 M $Na_3PO_4$ (sodium phosphate, 98%) in a DW : ethanol (1 : 9 vol%) mixture was dropped (10 μL $cm^{-2}$) on the photoanode and annealed at 300 °C for 30 min.

AQ-Modified carbon cathodes were synthesized *via* a simple drop-casting method. Typically, 3 mM AQ-2-COOH (anthraquinone-2-carboxylic acid, 98%) and 6.3 mg SWCNT (IL JIN Nanotech., ASA-100) as a supporter and 12 μL Nafion solution (5 wt% in a mixture of lower aliphatic alcohols and water (40%)) as a binder were dissolved and well dispersed in 1 mL MeCN (acetonitrile, anhydrous, 98%) by sonication. An aliquot of 40 μL solution was dropped on carbon paper substrates (CeTech Co., GDS210, 10 mm × 10 mm coating area (total 10 mm × 30 mm), FC international) and then dried at 80 °C for 10 min on a hot plate. The above drop-casting process was repeated up to 10 times to obtain the final AQ-modified carbon cathode (denoted as AQ-CNT/C). For comparison, a carbon cathode without AQ was also prepared using a solution containing SWCNT and Nafion only (denoted as CNT/C).

### (Photo)electrochemical measurements

The (photo)electrochemical performances of BVO, AQ-CNT/C, or the BVO‖AQ-CNT/C configuration were measured in a typical three electrode system with a two-compartment cell separated by a Nafion membrane (Nafion Membrane N117) containing 1 M $NaHCO_3$ (99.7–100.3%, pH ~ 7.8 adjusted by $HClO_4$) (see the PEC-I, EC-I, and PEC-II systems in Scheme 1). If necessary, the Nafion membrane was removed to carry out one-compartment cell experiments and a Pt electrode sputtered on an FTO substrate (20 mA for 30 s; Cressington 208HR) was adopted as a counter electrode. The solutions were purged with Ar (99.9%) or $O_2$ (99.9%) gas for at least 15 min prior to and during the measurements in the working (anodic) or counter (cathodic) electrode cells, respectively. If necessary, a two electrode system with a two-compartment cell was also adopted (see the PEC-III system in Scheme 1). For linear sweep voltammetry (LSV), the potential of the working electrode was swept from −0.5 to +1.5 V (*vs.* Ag/AgCl) at a scan rate of 50 mV $s^{-1}$ using an electrochemical workstation (VersaSTAT 3-400, Princeton Applied Research) in the dark or under AM 1.5G light (100 mW $cm^{-2}$). For chronoamperometry (CA), a constant potential of +0.34 V *vs.* Ag/AgCl (equivalent to +1.00 V *vs.* RHE) was applied to the working electrode. For Mott–Schottky analysis, the potential was swept from −0.5 to −0.1 V *vs.* Ag/AgCl at a frequency of 1 kHz in the dark. For electrochemical impedance spectroscopy (EIS) analysis, +0.34 V *vs.* Ag/AgCl with an AC voltage of 10 mV and a frequency ranging from 0.1 kHz to 0.01 Hz was applied to the working electrodes under irradiation. The measured potentials were converted to the corresponding potentials *vs.* RHE using the following equation: $V$ (*vs.* RHE) = $V$ (*vs.* Ag/AgCl) + 0.0591pH + 0.197.

While applying a constant potential to the working electrode, the amount of produced $H_2O_2$ was quantified in both the anode and cathode compartments using the iodometric titration method. Typically, 0.1 M $C_8H_5KO_4$ (potassium biphthalate, Alfa Aesar, 98%) solution and 0.4 M KI (potassium iodide, 99.5%) solution containing 0.06 M NaOH (sodium hydroxide, 1 M) and 0.1 mM $(NH_4)_2MoO_4$ (ammonium molybdate, 99%) were prepared in advance. A sample aliquot of 0.5 mL and 1.5 mL of purified water was mixed with both biphtalate (0.75 mL) and iodide solutions (0.75 mL), which was kept under vigorous stirring for 2 min before measuring the absorbance at 372 nm using a UV/visible spectrophotometer (Libra S22, Biochrom). The faradaic efficiency for $H_2O_2$ production was calculated based on the typical calculation formula (see page S14 in the ESI†). In addition, the headspace gaseous products ($O_2$ and $H_2$) in both cells were quantified using a gas chromatograph (GC, HP6890A) equipped with a thermal conductivity detector (TCD) and a 5 Å-molecular sieve column. Prior to irradiation, the solutions were purged with Ar gas in the working electrode cell for 30 min to remove dissolved oxygen. For electrochemical rotating disk electrode (RDE) voltammetry, a glassy carbon disk working electrode (3 mm diameter, ALS Co., no. 011169), a Pt wire counter electrode, and a Ag/AgCl reference electrode were placed in a single cell containing 0.1 M KOH (pH 13). For LSV, the potential of the working electrode was swept from −0.1 to −0.6 V (*vs.* Ag/AgCl) at a scan rate of 10 mV $s^{-1}$ using an electrochemical workstation (VersaSTAT 3-400, Princeton Applied Research) in the dark. The solutions were pre-purged with Ar gas for at least 15 min prior to and during the measurements. The rotation speed was varied from 400 to 2400 revolutions per minute (rpm) using a rotating ring disk electrode rotator (RRDE-3A, ALS Co., Ltd).

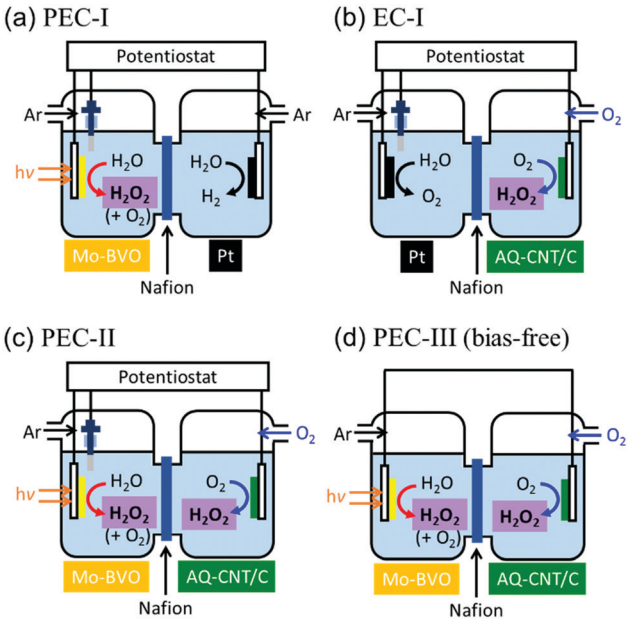


Scheme 1 Schematic illustration of (photo)electrochemical systems for (a) photoanodic production of $H_2O_2$ through water oxidation (PEC-I system) and (b) cathodic production of $H_2O_2$ through the ORR (EC-I system), (c) the combined system of photoanodic and cathodic production of $H_2O_2$ (PEC-II system), and (d) the combined two electrode system of photoanodic and cathodic production of $H_2O_2$ without an external bias (PEC-III system).

### Surface characterization

The morphology of the samples was analyzed by high-resolution field-emission scanning electron microscopy (HR-FE-SEM; JEOL JSM-7401F) at the National Institute for Nanomaterials Technology (Pohang, Korea). Surface elemental composition and chemical analysis were performed by X-ray photoelectron spectroscopy (XPS; Theta Probe AR-XPS system) using monochromated Al Kα radiation as an X-ray source (1486.6 eV, Busan Center, KBSI, Korea). X-ray diffraction (XRD) patterns were measured using Cu Kα radiation (RIGAKU D MAX 2500). The UV-visible absorption spectra of the BVO samples were obtained using a Shimadzu UV-2401PC spectrophotometer. The surface functional groups of the samples were analyzed by attenuated total reflectance Fourier transform infrared spectroscopy (ATR-FTIR; Thermo Scientific iS50) using a ZeSe crystal with a scan number of 100.

## Results and discussion

### Surface characterization of modified $BiVO_4$ and AQ-modified carbon electrodes

The optimized Mo-modified $BiVO_4$ (Mo-BVO) samples exhibited a porous structure, confirmed by SEM, with an average particle size of 60–70 nm and a thickness of ~130 nm (Fig. 1a and Fig. S1d, ESI†). The overall morphology of Mo-BVO changed only slightly from that of the bare BVO even with the addition of a high concentration of Mo (10 atom% in vanadium sites) (Fig. S1a, ESI†). $BiVO_4$ modified with other metal ions (W or Cr) also showed structures similar to that of Mo-BVO (Fig. S1, ESI†). The XRD patterns of the bare BVO samples exhibited typical monoclinic scheelite $BiVO_4$ peaks at $2\theta$ = 18.7, 28.8, 30.5, 34.5, 35.2, 39.8, 42.5, 46.7, 47.3, 50.3, and 53.3° for (110), (121), (040), (200), (002), (211), (051), (240), (042), (202), and (161), respectively (JCPDS ref. no. 14-0688), which is in good agreement with the literature (Fig. 1b and Fig. S2, ESI†).[38–40] However, the BVO samples modified with any metal (Mo, W, or Cr) exhibited patterns that differ from that of the bare BVO sample around 34–36°, where two individual peaks merge to form a single peak (Fig. 1b). This indicates the phase transition from monoclinic to tetragonal structure by the high concentration of metal ions contained in the BVO lattice.[41–43] In addition, separate XRD peaks of $MoO_3$, $WO_3$, or $Cr_2O_3$ were observed in each sample (Fig. S2, ESI†), which indicates that the metal doping level (10 atom%) is high enough to induce the formation of a separate metal oxide phase during the annealing process.

The bare and metal-modified BVO samples were analyzed by XPS to investigate the elemental compositions and the chemical states of the elements. The O1s band exhibited two binding energy peaks in all samples, which represent the lattice oxygen species ($O_{latt}$) and the adsorbed oxygen species ($O_{ads}$), at ~529.5 and ~532.3 eV, respectively (Fig. 1c).[44–46] All spectra for the metal-modified BVO samples exhibit a slight shift (~0.1 eV) to higher binding energy for $O_{latt}$, indicating the

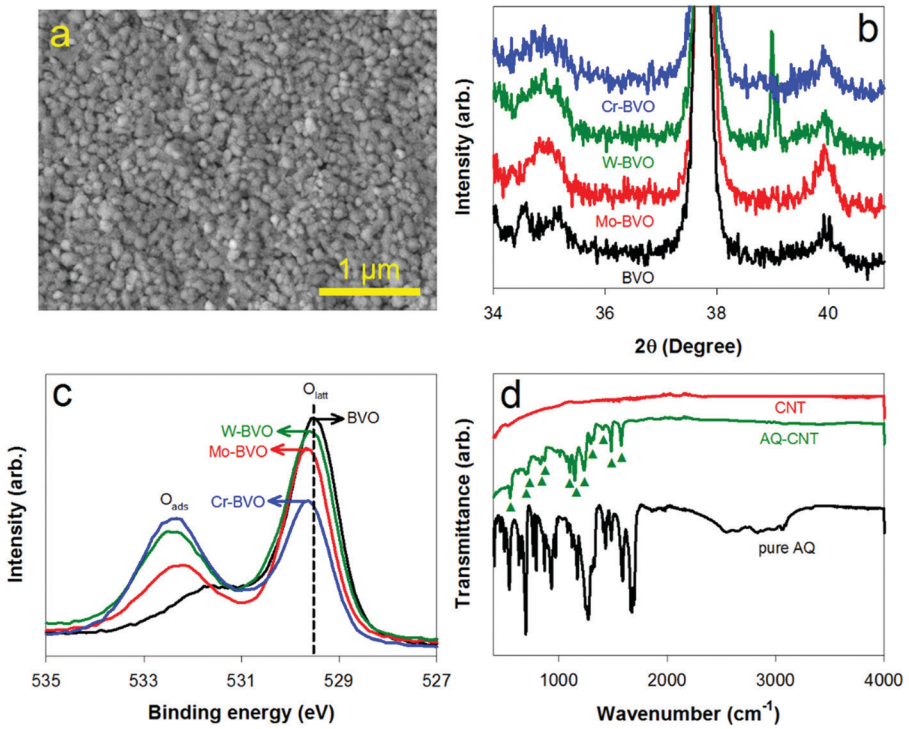


Fig. 1 (a) SEM image (top view) of $BiVO_4$ (BVO) modified with molybdenum (Mo-BVO). (b) Enlarged XRD patterns of bare BVO, Mo(10 atom%)-BVO, W(10 atom%)-BVO, and Cr(10 atom%)-BVO. See Fig. S2 (ESI†) for the full range of XRD patterns. (c) XPS spectra of O 1s for BVO, Mo-BVO, W-BVO, and Cr-BVO. See Fig. S3 (ESI†) for more XPS spectra (Bi 4f and V 2p). (d) FTIR spectra of SWCNT (CNT) and AQ-modified SWCNT (AQ-CNT). A pure AQ sample was also measured for comparison.

incorporation of metal ions into the $BiVO_4$ structures with oxygen bonding. The appearance of the $O_{ads}$ peak at ~532.3 eV is ascribed mainly to the surface hydroxyl groups, which can act as a hole scavenger in the photocatalytic reaction with producing hydroxyl radicals.[47,48] All metal-modified BVO samples exhibited stronger $O_{ads}$ peaks than bare BVO, which implies that more surface hole trapping sites on BVO are generated upon metal modification.[49,50] The metal-modified BVO samples also exhibited a binding energy shift to higher energy for the Bi 4f and V 2p peaks (Fig. S3a and b, ESI†), which was also reported in the literature.[51] This shift is ascribed to the fact that the electronegativity of hexavalent metal ions ($Mo^{6+}$, $W^{6+}$, and $Cr^{6+}$) is higher than that of the pentavalent metal ion ($V^{5+}$).[51] All XPS binding energies provided were corrected based on the maximum peak (C–C component) of the C 1s spectra (Fig. S3c, ESI†).

To characterize the AQ-modified carbon electrodes, the identification of AQ in the as-synthesized AQ-modified carbon samples was performed using Fourier transform infrared spectroscopy (FT-IR) on powder samples (Fig. 1d). The IR spectra of the AQ-modified SWCNT powder samples exhibited apparent peaks of AQ at 696, 1267, and 1666 $cm^{-1}$, which are not observed in the bare SWCNT powder. This confirms that AQ is well anchored on the SWCNT support.

### Photoelectrochemical activities of modified $BiVO_4$ (photoanodic $H_2O_2$ production through water oxidation)

The PEC activity of the bare BVO and Mo-BVO electrodes was first investigated using linear sweep voltammetry (LSV) in aqueous sodium bicarbonate solution (1 M; pH ~ 7.8 adjusted by $HClO_4$) that was purged with Ar gas (Fig. 2a). The bare BVO electrode exhibited an onset potential of 0.5 $V_{RHE}$ for $H_2O_2$ production from water oxidation with a faradaic efficiency (FE) lower than 25% for the tested potential range (+0.5 to +2.0 $V_{RHE}$) (Fig. S4, ESI†). The photocurrent generation was enhanced by the molybdenum (Mo) modification and the Mo-BVO containing 10 atom% Mo exhibited the highest photocurrent. When modifying BVO, metal ions with a valence state higher than $V^{5+}$, such as $Mo^{6+}$ and $W^{6+}$, are usually added as a dopant to substitute $V^{5+}$ sites in BVO to enhance the electrical conductivity by increasing the donor density.[37,52] The $H_2O_2$ production and FE on BVO were also enhanced with Mo modification in BVO, along with the photocurrent generation (Fig. 2a and Fig. S4, ESI†). Among various Mo concentrations, a typical concentration of 10 atom% in BVO exhibited the highest activity for photoanodic production of $H_2O_2$ with improved photocurrent generation.

To understand the effect of Mo modification on PEC, the PEC activity of BVO modified with other metal ions ($W^{6+}$ and $Cr^{6+}$ at 10 atom%) was also measured and compared with

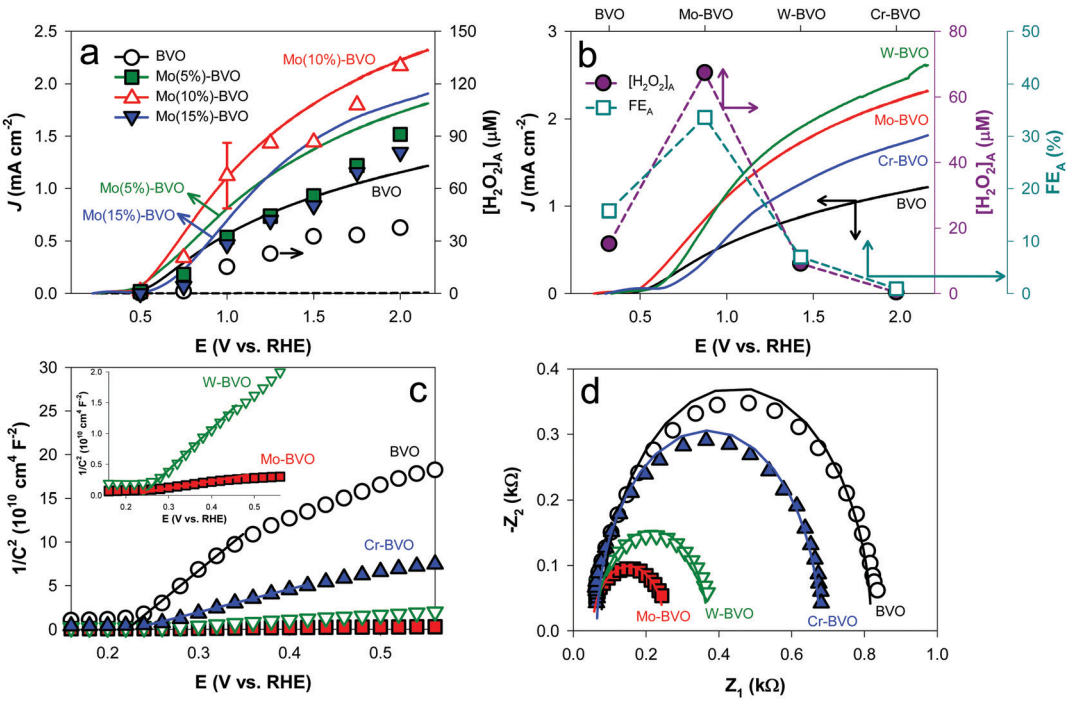


Fig. 2 (a) Linear sweep voltammograms (LSVs) for bare BVO and Mo-BVO with different concentrations of Mo. $[H_2O_2]_A$ is the concentration of $H_2O_2$ produced through the photoanodic reaction on bare BVO and Mo-BVO measured after 15 min reaction at each potential. (b) LSVs for BVO, Mo-BVO, W-BVO, and Cr-BVO (bottom, left axis) and $[H_2O_2]_A$ (top, right axis) with $FE_A$ (top, right-offset axis) for BVO, Mo-BVO, W-BVO, and Cr-BVO at an applied bias of 1.0 $V_{RHE}$ after 15 min. (c) Mott–Schottky (M–S) plots of BVO, Mo-BVO, W-BVO, and Cr-BVO measured at a fixed frequency of 1 kHz. (d) Nyquist plots of BVO, Mo-BVO, W-BVO, and Cr-BVO measured at an applied potential of 1.0 $V_{RHE}$ in 1 M $NaHCO_3$ solution (pH ~ 7.8) under AM 1.5G irradiation (100 mW $cm^{-2}$). The solid lines in (c) and (d) represent fitting of the plots. The Nyquist plots were fitted to the equivalent circuits (an RC circuit). See Table S1 (ESI†) for the parameter values estimated by the fitting. The PEC performances of bare and metal-modified BVO were measured (PEC-I system) in 1 M $NaHCO_3$ solution (pH ~ 7.8) in the dark or under AM 1.5G irradiation (100 mW $cm^{-2}$). The solution was pre-purged with Ar gas for at least 15 min prior to the experiments.

 

Table 1 Summary of the (photo)electrochemical $H_2O_2$ production performances of various electrode configurations

| Reaction type | Electrodes | Applied bias[a] | $H_2O_2$ production rate[b] ($\mu$mol min$^{-1}$ cm$^{-2}$) | FE (%) | $I_{ph}(20)/I_{ph}(0)$[c] |
|---|---|---|---|---|---|
| Photo-anodic | BVO | 1.0 | 0.03 | 15 | |
| | Mo-BVO | 1.0 | 0.13 | 35 | 0.13 |
| | W-BVO | 1.0 | 0.018 | 7 | |
| | Cr-BVO | 1.0 | 0.0007 | 0.9 | |
| | P-Mo-BVO | 1.0 | 0.21 | 46 | 0.98 |
| Cathodic[d] | CNT/C | 1.0 | 0.08 | 26 | |
| | AQ-CNT/C | 1.0 | 0.32 | 100 | |
| Dual | Mo-BVO‖CNT/C | 1.0 | 0.21 | | |
| | Mo-BVO‖AQ-CNT/C | 0.75 | 0.22 | | |
| | | 1.0 | 0.45 | | |
| | | 1.5 | 0.57 | | |
| | | 2.0 | 1.01 | | |
| | | Unbiased[e] | 0.11 | | |
| | P-Mo-BVO‖AQ-CNT/C | 1.0 | 0.66 | | |
| | | Unbiased[e] | 0.16 | | |

[a] A potential was applied to the photoanode in the three electrode system unless mentioned otherwise. [b] The $H_2O_2$ production rate was determined after 15 min reaction. [c] $I_{ph}(20)$: photocurrent after 20 h; $I_{ph}(0)$: initial photocurrent. [d] The cathodic reaction was conducted on a counter electrode with the Mo-BVO photoanode. [e] A two electrode system was adopted for this experiment with no potential bias between the electrodes.

Mo-BVO (Fig. 2b). The photocurrent generation was enhanced in all metal-modified BVO electrodes compared to bare BVO. The enhancement of the photocurrent for metal-modified BVO is ascribed to the higher electrical conductivity and lower charge transfer resistance, which were confirmed by Mott–Schottky (M–S) and electrochemical impedance spectroscopy (EIS) analysis, respectively (Fig. 2c, d and Table S1, ESI†). The electrical conductivity of the samples was estimated by the Mott–Schottky equation (see page S14 in the ESI†). However, the $H_2O_2$ production was enhanced only with the Mo-BVO electrode, while W-BVO and Cr-BVO exhibited suppressed activity for $H_2O_2$ production despite the enhanced photocurrent compared with bare BVO (Fig. 2b), and the results are summarized in Table 1. The $Mo^{6+}$ modification seems to play a unique role in enhancing the PEC production of $H_2O_2$.

To compare with the PEC production of $H_2O_2$, the PEC decomposition of $H_2O_2$ was further investigated in phosphate buffer solution in the absence of bicarbonate ions (Fig. 3). We observed that the bare and modified BVO did not produce $H_2O_2$ at all in the bicarbonate-free solution (data not shown). In the $H_2O_2$ decomposition experiments, a constant potential of 1.0 $V_{RHE}$ was applied to the bare and modified BVO working electrodes in 0.1 M phosphate buffer solution containing an initial concentration of 1 mM $H_2O_2$ (Fig. 3a). The decomposition of $H_2O_2$ was assessed over 3 h PEC reaction. The amounts of total charge ($Q_T$) that passed through the PEC cell were calculated in coulombs (C) for each photoanode based on its photocurrent generation (Fig. 3b). The amounts of $H_2O_2$ decomposition were divided by the total charge passed in the PEC cell (Fig. 3c). The amounts of $H_2O_2$ decomposition relative to the total charge ($-\Delta[H_2O_2]/Q_T$) were the lowest on the Mo-BVO electrode. Although the amounts of decomposed $H_2O_2$ were the lowest on the Cr-BVO electrode, the Cr-BVO electrode exhibited a negligible photocurrent during the measurement (see the inset of Fig. 3b). As the $H_2O_2$ molecule is a strong hole scavenger, it can be rapidly decomposed by reacting with holes on the photoanode surface.[53] Mo modification seems to be efficient in retarding the hole-mediated decomposition of $H_2O_2$, thereby enhancing the overall production of $H_2O_2$. We also examined the photoanodic $H_2O_2$ production using other semiconductor materials including $WO_3$, $TiO_2$, and $Fe_2O_3$ (Fig. S5, ESI†). However, all other materials exhibited lower FEs for photoanodic $H_2O_2$ production than Mo-BVO. In this regard, $BiVO_4$ seems to be the best base material among the materials we investigated for photoanodic $H_2O_2$ production.

### Electrochemical activities of AQ-modified carbon electrodes (cathodic $H_2O_2$ production through the ORR)

The electrochemical (EC) activity of the as-synthesized AQ-modified SWCNT on carbon paper (AQ-CNT/C) electrodes was also individually investigated by cyclic voltammetry (CV) with a Pt counter electrode in aqueous sodium bicarbonate solution (1 M; pH $\sim$ 7.8 adjusted by $HClO_4$), which was purged with Ar or $O_2$ gas (Fig. 4a). The CV scans for the AQ-CNT/C electrodes exhibit a typical pattern of the two-electron redox process of anthraquinone/anthrahydroquinone (AQ–AHQ), showing the reduction and oxidation peaks at 0.1 and 0.15 $V_{RHE}$, respectively.[33,54] These peaks do not appear for the bare carbon paper electrode (C) or the SWCNT-loaded carbon paper electrode (CNT/C). Under $O_2$ purging, AQ-CNT/C exhibited a current onset potential of $\sim$0.4 $V_{RHE}$ for the ORR while the CNT/C electrode did not exhibit such an ORR current peak. This indicates that AQ plays a critical role in the ORR process. The presence of AQ on the cathode surface markedly facilitated the interfacial charge transfer process as shown in EIS analysis (Fig. 4b). The charge transfer resistance can be determined by fitting the plots to the equivalent circuits (a simple RC model; Fig. S6, ESI†). The charge transfer resistance for AQ-CNT/C was lower than that for the other

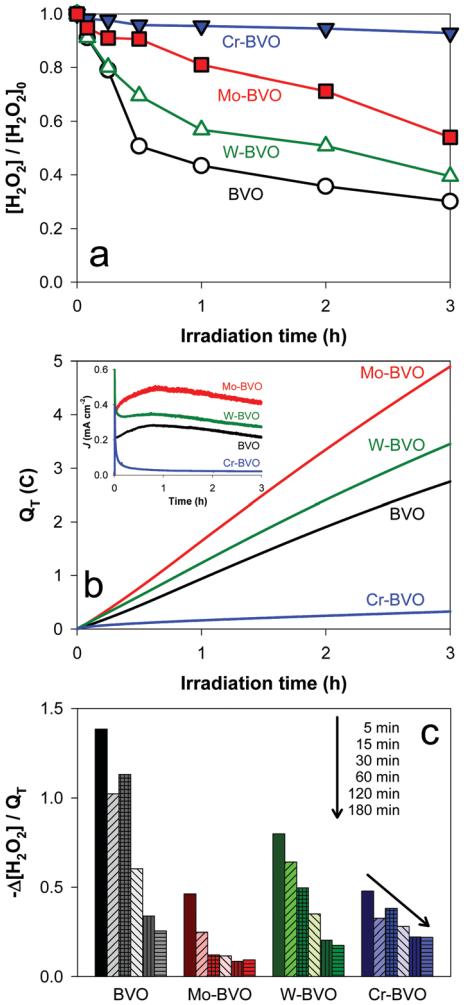


Fig. 3 (a) The PEC decomposition of $H_2O_2$ on BVO, Mo-BVO, W-BVO, and Cr-BVO. (b) Total charge ($Q_T$) passed through the circuit during the PEC reaction in (a). The inset shows the time-profiled photocurrents generated on BVO, Mo-BVO, W-BVO, and Cr-BVO. (c) The $H_2O_2$ decomposition divided by $Q_T$ ($-\Delta[H_2O_2]/Q_T$) for BVO, Mo-BVO, W-BVO, and Cr-BVO. The PEC performances of bare and metal-modified BVO were measured (PEC-I system) in 0.1 M sodium phosphate buffer solution (pH ~ 7) with 1 mM $H_2O_2$ under AM 1.5G irradiation (100 mW cm$^{-2}$) at an applied bias of 1.0 $V_{RHE}$. The solution was pre-purged with Ar gas for at least 15 min prior to the experiments.

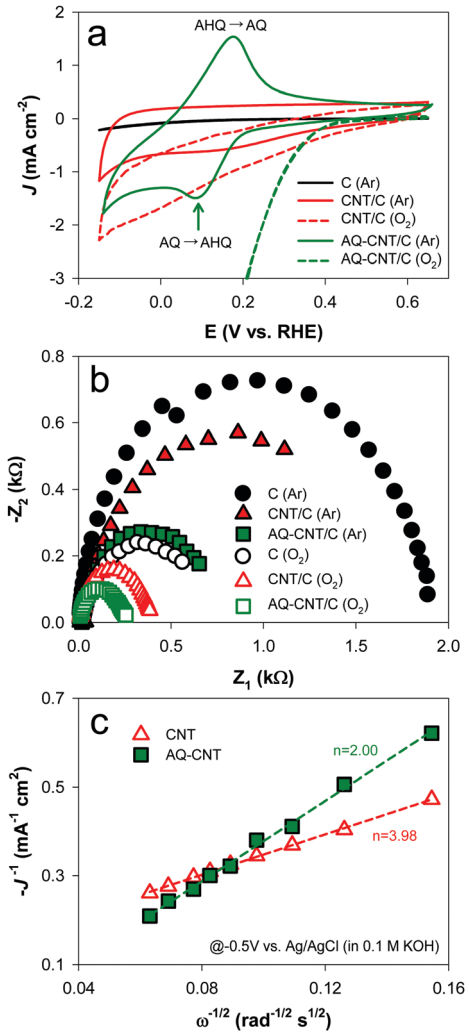


Fig. 4 (a) Cyclic voltammograms (CVs) of bare carbon paper substrate (C), SWCNT coated carbon paper (CNT/C), and AQ-modified SWCNT coated carbon paper (AQ-CNT/C) electrodes. (b) Nyquist plots of C, CNT/C, and AQ-CNT/C. EIS was conducted at an applied potential of −1.5 $V_{RHE}$. The EC performances of AQ-CNT/C were measured (EC-I system) in 1 M $NaHCO_3$ solution (pH ~ 7.8) in the dark. The solution was pre-purged with $O_2$ gas and Ar gas in the anode and cathode part, respectively, for at least 15 min prior to the experiments. (c) Koutecky–Levich plots of CNT and AQ-CNT powder from rotating disk electrode (RDE) measurements at an applied bias of −0.5 $V_{Ag/AgCl}$ in 0.1 M KOH pre-purged with $O_2$ gas. See Fig. S7 (ESI†) for the RDE current–potential curves.

electrodes (CNT/C or C) and further lowered by the presence of $O_2$. This indicates that AQ on the cathode can facilitate intramolecular electron transfer and that the ORR is more favored over the water reduction reaction on the AQ-loaded cathode.

The selectivity of the AQ-loaded electrode for $H_2O_2$ production *via* $O_2$ reduction was examined using the rotating disk electrode (RDE) technique. The RDE experiments were performed in an aqueous solution containing 0.1 M KOH as this is the condition usually employed for electrochemical ORR studies.[55,56] Koutecký–Levich (K–L) plots for the ORR on the RDE were compared for different samples (CNT and AQ-CNT) (Fig. 4c and Fig. S7, ESI†). The number $n$ of transferred electrons can be calculated from the K–L plots, which was found to be 4 and 2 for the CNT and AQ-CNT electrode, respectively. This indicates that the products of the ORR should be different on the CNT and AQ-CNT electrodes. The production of $H_2O_2$ through the ORR should be strongly favored on AQ-CNT through two-electron transfer whereas the ORR on the CNT electrode should generate $H_2O$ through four-electron transfer instead.

### Photoelectrochemical activities of the Mo-BVO‖AQ-CNT/C configuration (dual photoanodic and cathodic $H_2O_2$ production)

The PEC behavior of the combined configuration of the Mo-BVO and AQ-CNT/C electrodes for dual production of

 

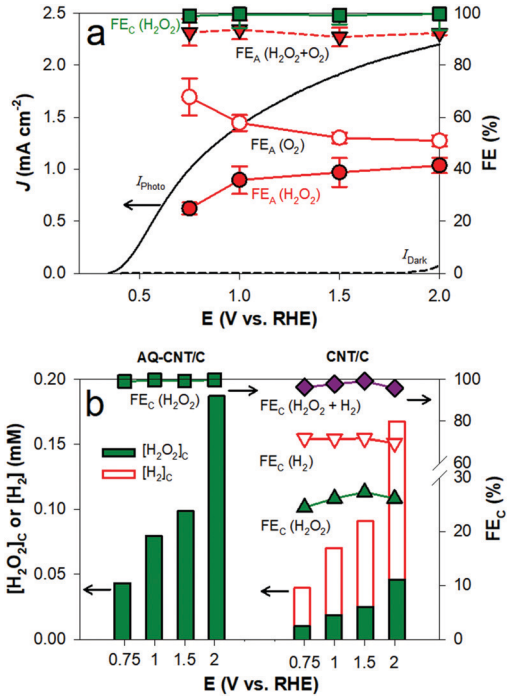


Fig. 5 (a) Linear sweep voltammograms (LSVs) for the Mo-BVO‖AQ-CNT/C configuration. Faradaic efficiencies (FEs) for $H_2O_2$ production (or $O_2$ evolution) are also shown. The amounts of produced $H_2O_2$ (or evolved $O_2$) from M-BVO and AQ-CNT/C were measured after 15 min reaction at each potential in a two-compartment cell (PEC-II system). $FE_A$ and $FE_C$ represent the faradaic efficiency of the photoanodic reaction (Mo-BVO) and cathodic reaction (AQ-CNT/C), respectively. (b) The cathodic $H_2O_2$ production (or $H_2$ evolution) and FEs for the Mo-BVO‖AQ-CNT/C and Mo-BVO‖CNT/C configurations in a two-compartment cell. $[H_2O_2]_C$ and $[H_2]_C$ were measured after 15 min reaction at each potential. The PEC performances of the Mo-BVO‖AQ-CNT/C configuration were measured (PEC-II system) in 1 M $NaHCO_3$ solution (pH ~ 7.8) under AM 1.5G irradiation (100 mW cm$^{-2}$). The solution was pre-purged with Ar gas and $O_2$ gas in the photoanode and cathode parts, respectively, for at least 15 min prior to the experiments.

$H_2O_2$ was examined across a range of potentials (Fig. 5a). The amounts of $H_2O_2$ produced and gaseous products ($O_2$ and $H_2$) evolved in each cell were measured by sampling from the solution and headspace, respectively. The FE values for each product were calculated by measuring the concurrent photocurrent. The FE values for $H_2O_2$ production on the Mo-BVO photoanode ($FE_A$ ($H_2O_2$)) varied from 20 to 40%, depending on the efficiency of the competitive $O_2$ evolution reaction. The sum of the FE values for $H_2O_2$ production ($FE_A$ ($H_2O_2$)) and $O_2$ evolution ($FE_A$ ($O_2$)) was near 100%. The FE values of slightly lower than 100% might be due to the immediate decomposition of *in situ* produced $H_2O_2$ on Mo-BVO (Fig. 3). On the other hand, the FE values for $H_2O_2$ generation on AQ-CNT/C ($FE_C$ ($H_2O_2$)) reached 100% over a wide potential range, and molecular $H_2$ was not evolved at all. As-synthesized C and CNT/C were also adopted as a counter electrode to examine the PEC activity with as-optimized Mo-BVO photoanodes (Fig. S8, ESI†). The photocurrent generation of Mo-BVO varied with different counter electrodes (AQ-CNT/C, CNT/C, and C), showing the highest performance with AQ-CNT/C counter electrodes under $O_2$ gas. To assess the selectivity of AQ for the ORR, the $H_2O_2$ production was examined between two different counter electrodes (AQ-CNT/C *vs.* CNT/C electrodes) (Fig. 5b). Various potentials were applied on the Mo-BVO photoanode (from 0.75 to 2 $V_{RHE}$), and the $H_2O_2$ and $H_2$ produced from the cathode were measured after 15 min. The amounts of $H_2O_2$ produced on the cathode were much higher in the presence of AQ, showing FE values of ~100 and ~30% for the AQ-CNT/C and CNT/C electrodes, respectively, and the results are also summarized in Table 1. In addition, $H_2$ was not produced on AQ-CNT/C at all, whereas the amount of $H_2$ produced on CNT/C was much higher than $H_2O_2$ with FE values of ~70%. This clearly indicates that AQ has a highly selective catalytic property for the ORR to produce $H_2O_2$. The low reactivity of the CNT/C electrode for oxygen reduction was shown in the CV in the experiment (Fig. 4a), which showed that the EC behavior of the CNT/C electrode under Ar or $O_2$ gas purging was not changed much.

### Enhanced PEC activities and durability of phosphate-treated Mo-modified $BiVO_4$ (P-Mo-BVO)

We demonstrated successful $H_2O_2$ production *via* a dual mechanism on the Mo-BVO‖AQ-CNT/C configuration, however Mo-BVO still suffers from low FEs for photoanodic $H_2O_2$ production with poor durability, which will be discussed later. To solve these issues, the surface of the Mo-BVO electrode was treated with phosphate (adsorbed). The current generation of Mo-BVO was enhanced by phosphate treatment at positive oxidation potentials (>2.5 $V_{RHE}$) under both dark and irradiation conditions (Fig. 6a). Similarly, it was also observed that the configuration of phosphate-treated Mo-BVO (P-Mo-BVO) and AQ-CNT/C electrodes exhibited enhanced photocurrent generation (Fig. 6b). The FE for photoanodic $H_2O_2$ production was also enhanced in the tested potential range (Fig. 6b), which clearly indicates the positive effect of surface phosphate treatment on Mo-BVO for $H_2O_2$ production. To find out the effect of phosphate treatment on Mo-BVO, the PEC decomposition of $H_2O_2$ was investigated on P-Mo-BVO (Fig. S9, ESI†). The amounts of $H_2O_2$ decomposition relative to the total charge were highly reduced by phosphate treatment on Mo-BVO, indicating that the surface phosphate could effectively hinder the surface adsorption of $H_2O_2$ molecules on the surface.[4] The time-profiled production of $H_2O_2$ on the P-Mo-BVO with AQ-CNT/C configuration was further examined to test the stability of the reaction in the two-compartment cell (Fig. 6c). The experiments were performed at a constant potential of 1 $V_{RHE}$ applied on Mo-BVO for 5 h under AM 1.5G irradiation (100 mW cm$^{-2}$). The photocurrent generation of the P-Mo-BVO‖AQ-CNT/C configuration was relatively maintained during 5 h running whereas that of the Mo-BVO‖AQ-CNT/C or Mo-BVO‖CNT/C configuration exhibited a gradual decrease with time, and as a result the overall $H_2O_2$ production was highly enhanced with the P-Mo-BVO‖AQ-CNT/C configuration.

The durability of the photoanode itself was also examined and compared between Mo-BVO and P-Mo-BVO in the long-term

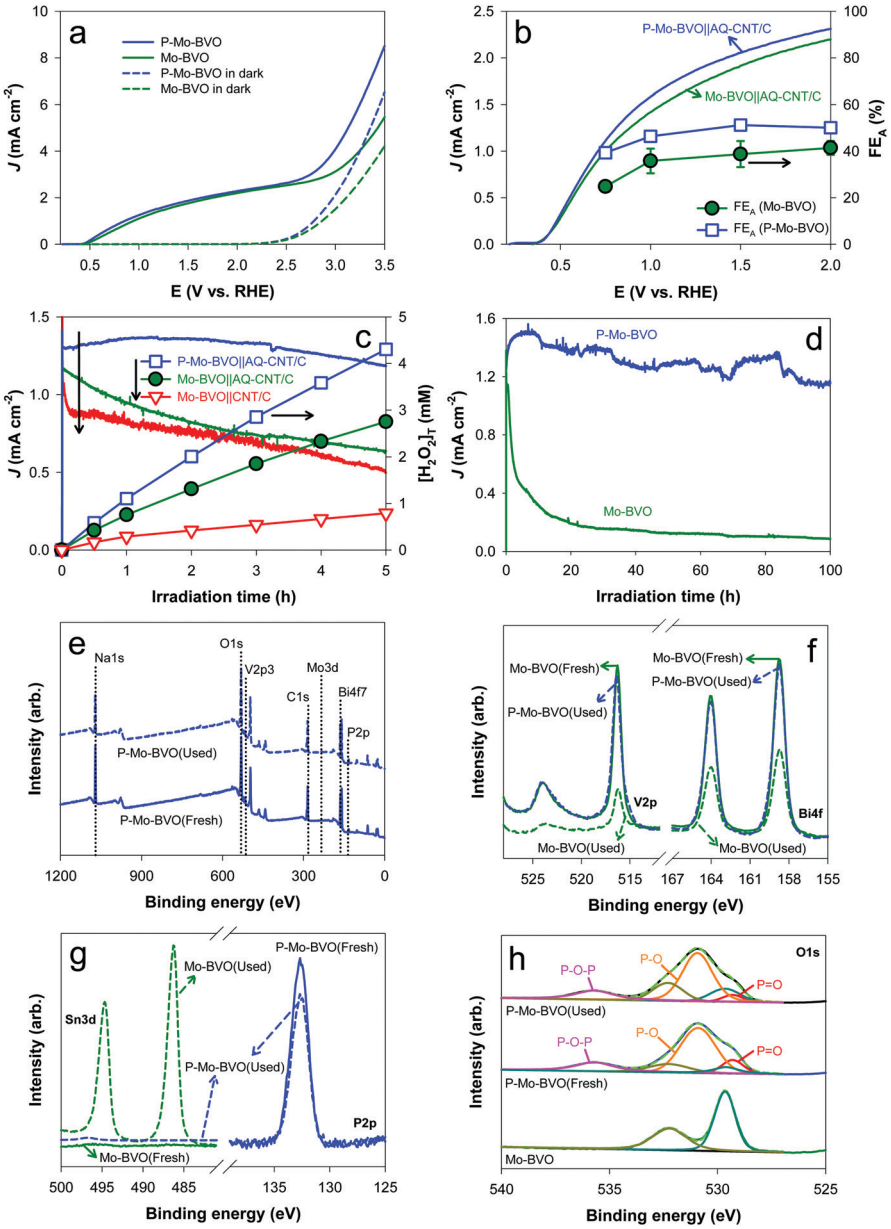


Fig. 6 (a) Linear sweep voltammograms (LSVs) for Mo-BVO and P-Mo-BVO in the dark or under irradiation conditions. (b) LSVs for the Mo-BVO‖AQ-CNT/C and P-Mo-BVO‖AQ-CNT/C configurations. Faradaic efficiencies for photoanodic $H_2O_2$ production ($FE_A$) were measured after 15 min reaction at each potential. (c) Time-profiled $H_2O_2$ production in the P-Mo-BVO‖AQ-CNT/C configuration at 1.0 $V_{RHE}$ over 5 h in a two-compartment cell. The PEC performances of the P-Mo-BVO‖AQ-CNT/C configuration were measured (PEC-II system) in 1 M $NaHCO_3$ solution (pH ~ 7.8) under AM 1.5G irradiation (100 mW $cm^{-2}$). The solution was pre-purged with Ar gas and $O_2$ gas in the photoanode and cathode parts, respectively, for at least 15 min prior to the experiments. For comparison, the Mo-BVO‖AQ-CNT/C and Mo-BVO‖CNT/C configurations were also compared. (d) The time-profiled photocurrent generation on Mo-BVO and P-Mo-BVO over 100 h. The PEC performances of Mo-BVO and P-Mo-BVO were measured (PEC-I system) in 1 M $NaHCO_3$ solution (pH ~ 7.8) under AM 1.5G irradiation (100 mW $cm^{-2}$). The solution was pre-purged with Ar gas in the photoanode part for at least 15 min prior to the experiments. XPS spectra for Mo-BVO (fresh and used) and P-Mo-BVO (fresh and used) of (e) survey, (f) Bi 4f and V 2p, (g) P 2p and Sn 3d, and (h) O 1s.

over 100 h (Fig. 6d). The photocurrent of the untreated Mo-BVO photoanode was gradually reduced and became negligible within 20 h, indicating possible dissolution of $BiVO_4$.[57] However, the photocurrent of the P-Mo-BVO photoanode remained 90% of its initial value over 100 h, which indicates that the surface phosphate-treatment played an important role in enhancing the stability of the photoanode. Since the long-term durability of $BiVO_4$ in an electrolyte containing bicarbonate for $H_2O_2$ production systems has not been investigated so far, the development of P-Mo-BVO as a practical and durable photoanode represents a significant advance for sustainable PEC $H_2O_2$ production.

To understand the origin of the phosphate effect, the behaviors of the Mo-BVO and P-Mo-BVO electrodes were further compared by measuring the variation of the open circuit potential (OCP) upon spiking $H_2O_2$ under both dark and irradiation

 

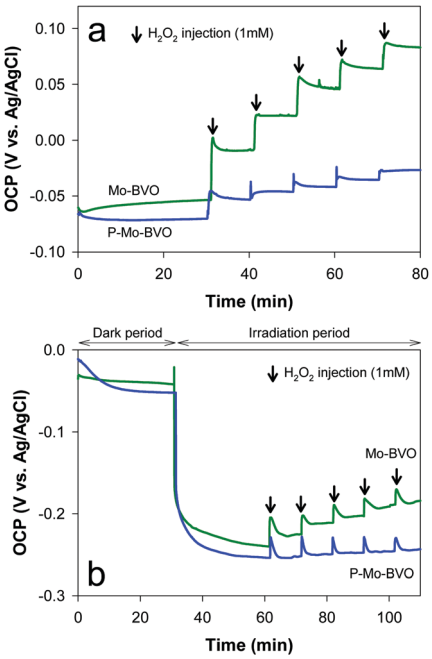


Fig. 7 Open circuit potential (OCP) of Mo-BVO and P-Mo-BVO (a) in the dark and (b) under irradiation conditions. $H_2O_2$ was spiked during the OCP measurements. The total concentration of $H_2O_2$ in the solution increased by 1 mM upon each spike. The PEC performances of bare Mo-BVO and P-Mo-BVO were measured (PEC-I system) in 1 M $NaHCO_3$ solution (pH ~ 7.8) under AM 1.5G irradiation (100 mW $cm^{-2}$). The solution was pre-purged with Ar gas for at least 15 min prior to the experiments.

conditions (Fig. 7). When $H_2O_2$ was injected into the electrolyte solution at the open-circuit condition, the OCP of Mo-BVO was significantly shifted to the positive direction while that of P-Mo-BVO was much less affected. The change of the OCP indicates charge transfer between the electrode surface and adsorbed molecules (in this case, $H_2O_2$).[58] That is, the $H_2O_2$-induced positive shift of the OCP implies that the introduction of $H_2O_2$ induces the oxidative dissolution of the BVO electrode.[57] The fact that P-Mo-BVO exhibited a much smaller change of the OCP upon $H_2O_2$ addition implies that the surface phosphate treatment inhibits the interaction between Mo-BVO and $H_2O_2$ (with retarding the PEC decomposition of $H_2O_2$ as shown in Fig. S9a, ESI†) and subsequently retards the $H_2O_2$-induced oxidative dissolution of BVO. Therefore, further reactions of *in situ* photogenerated $H_2O_2$ with the Mo-BVO electrode material should be hindered by the phosphate treatment of the photoanode. This should explain why P-Mo-BVO is more stable than Mo-BVO during prolonged PEC operation.

The durability of $BiVO_4$ was further examined by surface analysis after continuous PEC reactions for 100 h. The morphology of $BiVO_4$ was significantly changed, showing that the porous structure of $BiVO_4$ was seriously damaged and even the bare FTO substrate was exposed at the surface (compare Fig. S10c and d, ESI†), whereas the morphology of phosphate-treated $BiVO_4$ remained stable (Fig. S10a and b, ESI†). The XPS survey spectra also show that the surface elemental compositions of P-Mo-BVO were not changed even after 100 h PEC operation (Fig. 6e) and that the cation (sodium) ions associated with the phosphate remained stable during the PEC operation, which reconfirms the PEC stability of the phosphate-treated Mo-BVO electrode. Comparison of the Bi 4f and V 2p XPS spectra shows clearly that the intensities of both peaks in Mo-BVO were markedly reduced after 100 h PEC operation whereas the XPS spectra for P-Mo-BVO remained unchanged, indicating that the dissolution of $BiVO_4$ was prevented by phosphate treatment (Fig. 6f). The Mo 3d XPS spectra also exhibited similar results, showing that the peak intensity for Mo-BVO was reduced after the PEC reactions (Fig. S10e, ESI†). The dissolution of $BiVO_4$ induced the exposure of the bare FTO substrate, which was also confirmed by XPS analysis that shows the appearance of the Sn 3d XPS peak on Mo-BVO after the PEC reactions (Fig. 6g). On the contrary, P-Mo-BVO maintained its composition even after 100 h PEC reaction with not exposing the FTO substrate and retaining P elements on its surface (Fig. 6g). The phosphate speciation on P-Mo-BVO could be characterized by XPS O 1s band analysis (Fig. 6h). The phosphate treatment clearly induced additional peaks in the O 1s band in comparison with bare Mo-BVO, which are attributed to a double bonded oxygen with phosphorus (P═O; non-bridging oxygen), an oxygen bound to the surface of Mo-BVO (P-O; non-bridging oxygen), and an oxygen bonded with two phosphorus atoms (P–O–P; bridging oxygen) at 529.3, 530.9, and 535.7 eV, respectively.[59] In addition, the P 2p XPS spectra for both the fresh and used P-Mo-BVO samples show the typical characteristic of a $PO_4$-tetrahedral structure at 132.5 eV (Fig. 6g).[60,61]

Finally, we tested the production of $H_2O_2$ on the two electrode system without an external potential bias (the PEC-III system). Comparing the LSV scans of the C, CNT/C, AQ-CNT/C, Mo-BVO, and P-Mo-BVO electrodes that were conducted separately on a three-electrode system, we found that the photocurrent of P-Mo-BVO and the current of AQ-CNT/C have an intersection (operation) point at 0.19 mA and a potential of 0.45 $V_{RHE}$, indicating that the configuration can be operated without an external bias (Fig. 8a). The photocurrent generation of P-Mo-BVO (or Mo-BVO) and AQ-CNT/C (or CNT/C, C) in a two-electrode system was examined by applying a constant potential of 0 V between the electrodes (which is equivalent to a system with no external bias) (Fig. 8b). The Mo-BVO coupled with C, CNT/C, and AQ-CNT/C and P-Mo-BVO coupled with AQ-CNT/C configurations exhibited a photocurrent generation of ~0.01, ~0.70, ~0.15, and ~0.19 mA, respectively. The time-profiled dual PEC production of $H_2O_2$ on the Mo-BVO‖AQ-CNT/C and P-Mo-BVO‖AQ-CNT/C configurations was successfully demonstrated over 5 h under the external bias-free condition (Fig. 8c). $H_2O_2$ was produced on both electrodes, with a net $H_2O_2$ production rate of 0.11 and 0.16 μmol $min^{-1}$ $cm^{-2}$, respectively, and the solar-to-$H_2O_2$ conversion efficiency for the system (P-Mo-BVO‖AQ-CNT/C) under the external bias-free condition was determined to be 0.27%. It should be also noted that the photocurrent rapidly declined in Mo-BVO‖AQ-CNT/C but was maintained in the P-Mo-BVO‖AQ-CNT/C configuration. The PEC performances of the various electrode configurations tested in this work are summarized in Table 1.

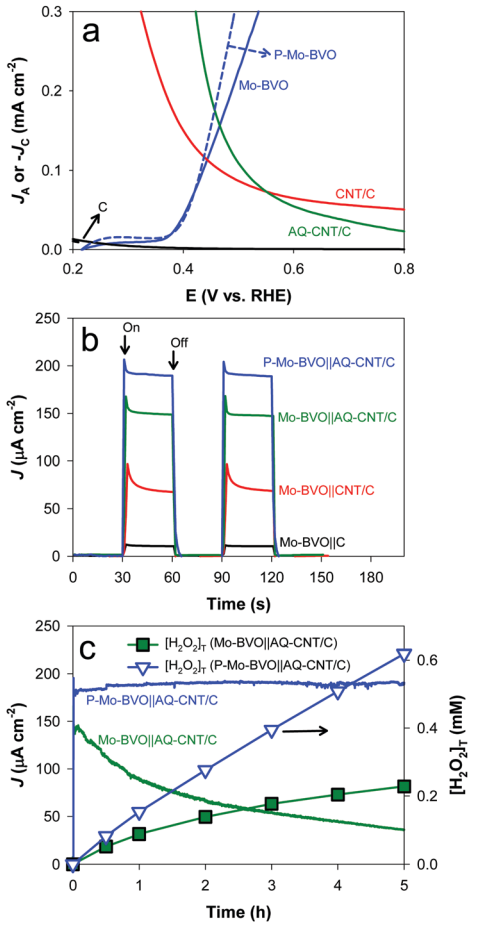


Fig. 8 (a) Linear sweep voltammograms (LSVs) of P-Mo-BVO, Mo-BVO, C, CNT/C, and AQ-CNT/C. The PEC performances of P-Mo-BVO, Mo-BVO, C, CNT/C, and AQ-CNT/C were measured (PEC-I or EC-I system) in 1 M $NaHCO_3$ solution (pH ~ 7.8) under AM 1.5G irradiation (100 mW cm$^{-2}$). The solution was pre-purged with Ar gas or $O_2$ gas for at least 15 min prior to the experiments. (b) Time-profiled photocurrents for the P-Mo-BVO with AQ-CNT/C and Mo-BVO with C, CNT/C, or AQ-CNT/C configurations in a two electrode system without an external bias. (c) Time-profiled $H_2O_2$ production for the P-Mo-BVO or Mo-BVO with AQ-CNT/C configuration over 5 h in a two electrode system under the external bias-free condition. The PEC performances of the P-Mo-BVO (or Mo-BVO)‖AQ-CNT/C (CNT/C or C) configuration were measured (PEC-III system) in 1 M $NaHCO_3$ solution (pH ~ 7.8) under AM 1.5G irradiation (100 mW cm$^{-2}$). The solution was pre-purged with Ar gas and $O_2$ gas in the photoanode and cathode parts, respectively, for at least 15 min prior to the experiments.

In addition, these performances and durability are also compared to those in previous studies (see Table S2, ESI†).

## Conclusions

Most studies of electrochemical, PEC, and photocatalytic production of $H_2O_2$ have employed the cathodic process of $O_2$ reduction. In this work, PEC $H_2O_2$ production using dual electrode processes was proposed and explored by combining a photoanode of modified $BiVO_4$ (BVO) and an anthraquinone-modified CNT cathode (AQ-CNT/C). The dual electrode process should utilize the photocurrent more efficiently for $H_2O_2$ production since a single charge pass in the PEC cell carries out double generation of $H_2O_2$ on both the photoanode and cathode. Although dual electrode processes (employing a BVO photoanode) for PEC $H_2O_2$ production have been previously reported, this study developed a highly durable and efficient photoanode and a highly selective cathode, which are combined to construct a practical and robust PEC system for sustained $H_2O_2$ production. The introduction of Mo dopants into BVO along with the phosphate treatment of the BVO surface (P-Mo-BVO) markedly enhanced the anodic $FE_a$ of $H_2O_2$ production (40-50%) and slowed the $H_2O_2$ decomposition kinetics. In addition, P-Mo-BVO is highly durable during the PEC reaction over 100 h (90% photocurrent maintained) while bare Mo-BVO experiences the rapid decline of the photocurrent (80% reduction in 12 h) during irradiation with the accompanying dissolution of $BiVO_4$. As for the cathode part, anchoring AQ on the CNT electrode dramatically enhanced the selectivity of $H_2O_2$ to an $FE_c$ of 100% through the ORR with suppressing $H_2$ production completely. As a result, the combined configuration of P-Mo-BVO and AQ-CNT/C successfully achieved the PEC production of $H_2O_2$ under both biased and unbiased conditions. This dual PEC approach can be employed as an ideal strategy for sustainable production of $H_2O_2$ as a solar fuel, which should maximize the photocurrent utilization efficiency under solar irradiation conditions. However, the challenging part is the concentration of a milli-molar level of photogenerated $H_2O_2$ for practical utilization, which should cost additional energy. An ideal solution should be the use of the dilute $H_2O_2$ solution as is. The most plausible application is to employ dilute $H_2O_2$ directly as an oxidant for environmental remediation such as Fenton oxidation, disinfection, and other advanced oxidation processes.

## Conflicts of interest

There are no conflicts to declare.

## Acknowledgements

This research was financially supported by the Global Research Laboratory (GRL) Program (NRF-2014K1A1A2041044), Basic Science Research Program (NRF-2017R1A2B2008952), and Basic Research Lab (BRL) Program (NRF-2018R1A4A1022194), which were funded by the Korea government (MSIT) through the National Research Foundation (NRF).

## References

1 A. D. Bokare and W. Choi, *J. Hazard. Mater.*, 2014, **275**, 121–135.
2 S. Fukuzumi and Y. Yamada, *ChemElectroChem*, 2016, **3**, 1978–1989.
3 D. Kim, K. K. Sakimoto, D. C. Hong and P. D. Yang, *Angew. Chem., Int. Ed.*, 2015, **54**, 3259–3266.

 

4 G. H. Moon, W. Kim, A. D. Bokare, N. E. Sung and W. Choi, *Energy Environ. Sci.*, 2014, **7**, 4023–4028.
5 S. Fukuzumi, Y. Yamada and K. D. Karlin, *Electrochim. Acta*, 2012, **82**, 493–511.
6 G. H. Moon, M. Fujitsuka, S. Kim, T. Majima, X. Wang and W. Choi, *ACS Catal.*, 2017, **7**, 2886–2895.
7 S. Kim, G. H. Moon, H. Kim, Y. Mun, P. Zhang, J. Lee and W. Choi, *J. Catal.*, 2018, **357**, 51–58.
8 C. M. Sanchez-Sanchez and A. J. Bard, *Anal. Chem.*, 2009, **81**, 8094–8100.
9 S. Siahrostami, A. Verdaguer-Casadevall, M. Karamad, D. Deiana, P. Malacrida, B. Wickman, M. Escudero-Escribano, E. A. Paoli, R. Frydendal, T. W. Hansen, I. Chorkendorff, I. E. L. Stephens and J. Rossmeisl, *Nat. Mater.*, 2013, **12**, 1137–1143.
10 S. Yang, A. Verdaguer-Casadevall, L. Arnarson, L. Silvio, V. Colic, R. Frydendal, J. Rossmeisl, I. Chorkendorff and I. E. L. Stephens, *ACS Catal.*, 2018, **8**, 4064–4081.
11 K. Mase, M. Yoneda, Y. Yamada and S. Fukuzumi, *Nat. Commun.*, 2016, **7**, 11470.
12 K. Fuku and K. Sayama, *Chem. Commun.*, 2016, **52**, 5406–5409.
13 K. Fuku, Y. Miyase, Y. Miseki, T. Gunji and K. Sayama, *RSC Adv.*, 2017, **7**, 47619–47623.
14 X. J. Shi, Y. R. Zhang, S. Siahrostami and X. L. Zheng, *Adv. Energy Mater.*, 2018, **8**, 1801158.
15 K. Fuku, Y. Miyase, Y. Miseki, T. Funaki, T. Gunji and K. Sayama, *Chem. – Asian J.*, 2017, **12**, 1111–1119.
16 J. Zhang, X. Chang, Z. Luo, T. Wang and J. Gong, *Chem. Commun.*, 2018, **54**, 7026–7029.
17 X. Shi, S. Siahrostami, G.-L. Li, Y. Zhang, P. Chakthranont, F. Studt, T. F. Jaramillo, X. Zheng and J. K. Nørskov, *Nat. Commun.*, 2017, **8**, 701.
18 Z. Li, W. Luo, M. Zhang, J. Feng and Z. Zou, *Energy Environ. Sci.*, 2013, **6**, 347–370.
19 J. W. Ager, M. R. Shaner, K. A. Walczak, I. D. Sharp and S. Ardo, *Energy Environ. Sci.*, 2015, **8**, 2811–2824.
20 M. Faraji, M. Yousefi, S. Yousefzadeh, M. Zirak, N. Naseri, T. H. Jeon, W. Choi and A. Z. Moshfegh, *Energy Environ. Sci.*, 2019, **12**, 59–95.
21 T. H. Jeon, G. H. Moon, H. Park and W. Choi, *Nano Energy*, 2017, **39**, 211–218.
22 H. I. Kim, D. Monllor-Satoca, W. Kim and W. Choi, *Energy Environ. Sci.*, 2015, **8**, 247–257.
23 W. Kim, T. Tachikawa, D. Monllor-Satoca, H. I. Kim, T. Majima and W. Choi, *Energy Environ. Sci.*, 2013, **6**, 3732–3739.
24 X. J. Shi, S. Siahrostami, G. L. Li, Y. R. Zhang, P. Chakthranont, F. Studt, T. F. Jaramillo, X. L. Zheng and J. K. Nørskov, *Nat. Commun.*, 2017, **8**, 701.
25 S. Siahrostami, G. L. Li, V. Viswanathan and J. K. Nørskov, *J. Phys. Chem. Lett.*, 2017, **8**, 1157–1160.
26 J. M. Campos-Martin, G. Blanco-Brieva and J. L. G. Fierro, *Angew. Chem., Int. Ed.*, 2006, **45**, 6962–6984.
27 J. K. Edwards and G. J. Hutchings, *Angew. Chem., Int. Ed.*, 2008, **47**, 9192–9198.
28 H. Shang, H. J. Zhou, W. H. Zhang and K. L. Zhang, *Can. J. Chem. Eng.*, 2011, **89**, 1296–1302.
29 S. X. Lu, Z. T. Mi, L. Wang, Y. Q. Wang, Z. H. Zhu and S. B. Fu, *Chem. Eng. Sci.*, 2005, **60**, 6298–6306.
30 A. Verdaguer-Casadevall, D. Deiana, M. Karamad, S. Siahrostami, P. Malacrida, T. W. Hansen, J. Rossmeisl, I. Chorkendorff and I. E. L. Stephens, *Nano Lett.*, 2014, **14**, 1603–1608.
31 Y. Jiang, P. Ni, C. Chen, Y. Lu, P. Yang, B. Kong, A. Fisher and X. Wang, *Adv. Energy Mater.*, 2018, **8**, 1801909.
32 L. Dai, Y. Xue, L. Qu, H.-J. Choi and J.-B. Baek, *Chem. Rev.*, 2015, **115**, 4823–4892.
33 A. Sarapuu, K. Vaik, D. J. Schiffrin and K. Tammeveski, *J. Electroanal. Chem.*, 2003, **541**, 23–29.
34 M. Kullapere and K. Tammeveski, *Electrochem. Commun.*, 2007, **9**, 1196–1201.
35 K. Vaik, A. Sarapuu, K. Tammeveski, F. Mirkhalaf and D. J. Schiffrin, *J. Electroanal. Chem.*, 2004, **564**, 159–166.
36 T. H. Jeon, W. Choi and H. Park, *Phys. Chem. Chem. Phys.*, 2011, **13**, 21392–21401.
37 H. W. Jeong, T. H. Jeon, J. S. Jang, W. Choi and H. Park, *J. Phys. Chem. C*, 2013, **117**, 9104–9112.
38 E. A. Mohamed, Z. N. Zahran and Y. Naruta, *J. Mater. Chem. A*, 2017, **5**, 6825–6831.
39 S. K. Cho, H. S. Park, H. C. Lee, K. M. Nam and A. J. Bard, *J. Phys. Chem. C*, 2013, **117**, 23048–23056.
40 B.-Y. Cheng, J.-S. Yang, H.-W. Cho and J.-J. Wu, *ACS Appl. Mater. Interfaces*, 2016, **8**, 20032–20039.
41 W. J. Jo, H. J. Kang, K.-J. Kong, Y. S. Lee, H. Park, Y. Lee, T. Buonassisi, K. K. Gleason and J. S. Lee, *Proc. Natl. Acad. Sci. U. S. A.*, 2015, **112**, 13774–13778.
42 S. Usai, S. Obregón, A. I. Becerro and G. Colón, *J. Phys. Chem. C*, 2013, **117**, 24479–24484.
43 S. Ikeda, T. Kawaguchi, Y. Highchi, N. Kawasaki, T. Harada, M. Remeika, M. M. Islam and T. Sakurai, *Front. Chem.*, 2018, **6**, 266.
44 Y. Zhang, D. Wang, X. Zhang, Y. Chen, L. Kong, P. Chen, Y. Wang, C. Wang, L. Wang and Y. Liu, *Electrochim. Acta*, 2016, **195**, 51–58.
45 L. Yang, Y. Xiong, W. Guo, J. Guo, D. Gao, Y. Zhang and P. Xiao, *Electrochim. Acta*, 2017, **256**, 268–277.
46 L. Chen, D. Meng, X. Wu, A. Wang, J. Wang, M. Yu and Y. Liang, *RSC Adv.*, 2016, **6**, 52300–52309.
47 L. Shan, H. Liu and G. Wang, *J. Nanopart. Res.*, 2015, **17**, 181.
48 S. Guo, X. Li, H. Wang, F. Dong and Z. Wu, *J. Colloid Interface Sci.*, 2012, **369**, 373–380.
49 H. Jiang, D. Hongxing, M. Xue, L. Zhang, D. Jiguang and J. Kemeng, *Chin. J. Catal.*, 2011, **32**, 939–949.
50 M. Wang, Y. Che, C. Niu, M. Dang and D. Dong, *J. Hazard. Mater.*, 2013, **262**, 447–455.
51 M.-W. Kim, K. Kim, T. Y. Ohm, B. Joshi, E. Samuel, M. T. Swihart, H. Yoon, H. Park and S. S. Yoon, *J. Alloys Compd.*, 2017, **726**, 1138–1146.
52 H. S. Park, K. E. Kweon, H. Ye, E. Paek, G. S. Hwang and A. J. Bard, *J. Phys. Chem. C*, 2011, **115**, 17870–17879.
53 H. Dotan, K. Sivula, M. Grätzel, A. Rothschild and S. C. Warren, *Energy Environ. Sci.*, 2011, **4**, 958–964.
54 K. Tammeveski, K. Kontturi, R. J. Nichols, R. J. Potter and D. J. Schiffrin, *J. Electroanal. Chem.*, 2001, **515**, 101–112.

55 Y. Liang, Y. Li, H. Wang, J. Zhou, J. Wang, T. Regier and H. Dai, *Nat. Mater.*, 2011, **10**, 780–786.
56 K. Gong, F. Du, Z. Xia, M. Durstock and L. Dai, *Science*, 2009, **323**, 760–764.
57 D. K. Lee and K.-S. Choi, *Nat. Energy*, 2018, **3**, 53.
58 D. H. Kim, G. H. Moon, M. S. Koo, H. I. Kim and W. Choi, *Appl. Catal., B*, 2020, **260**, 118146.
59 B. Fleutot, B. Pecquenard, H. Martinez, M. Letellier and A. Levasseur, *Solid State Ionics*, 2011, **186**, 29–36.
60 S. Leroy, F. Blanchard, R. Dedryvere, H. Martinez, B. Carré, D. Lemordant and D. Gonbeau, *Surf. Interface Anal.*, 2005, **37**, 773–781.
61 R. Jonsson, O. Mihai, J. Woo, M. Skoglundh, E. Olsson, M. Berggrund and L. Olsson, *Catalysts*, 2018, **8**, 155.